

# Variational State-Space Models for Localisation and Dense 3D Mapping in 6 DoF

Atanas Mirchev<sup>†</sup>, Baris Kayalibay<sup>†</sup>, Patrick van der Smagt<sup>‡</sup> and Justin Bayer<sup>†</sup>

Machine Learning Research Lab, Volkswagen Group  
80805, Munich, Germany

<sup>†</sup>{firstname.lastname}@argmax.ai

<sup>‡</sup>smagt@argmax.ai

**Abstract**—We solve the problem of 6-DoF localisation and 3D dense reconstruction in spatial environments as approximate Bayesian inference in a deep generative approach which combines learned with engineered models. This principled treatment of uncertainty and probabilistic inference overcomes the shortcoming of current state-of-the-art solutions to rely on heavily engineered, heterogeneous pipelines. Variational inference enables us to use neural networks for system identification, while a differentiable raycaster is used for the emission model. This ensures that our model is amenable to end-to-end gradient-based optimisation. We evaluate our approach on realistic unmanned aerial vehicle flight data, nearing the performance of a state-of-the-art visual inertial odometry system. The applicability of the learned model to downstream tasks such as generative prediction and planning is investigated.

## I. INTRODUCTION

Probabilistic generative models [Koller and Friedman, 2009] offer principled inference, predictions for control and uncertainty treatment. They are a natural fit for the modelling of moving agents, which revolves around estimating their pose and their surroundings, captured by the simultaneous localisation and mapping (SLAM) problem [Durrant-Whyte et al., 1996]. In recent years, researchers have made considerable progress in solving the SLAM task [Forster et al., 2014, Mur-Artal and Tardós, 2017, Engel et al., 2018, Qin et al., 2018]. Modern SLAM and visual odometry systems do not necessarily follow the generative framework, but have been shown to be an effective, real-time solution under moderate environment conditions. However, they are often built with heterogeneous modules optimised for different objectives, combining feature extractors [Lowe, 1999, Bay et al., 2006, Rublee et al., 2011], bundle adjustment [Triggs et al., 1999], pose-graph optimisation and BoW (Bag of Words) loop closure [Gálvez-López and Tardós, 2012]. This makes the tight integration of learning challenging. For the sake of efficiency, parameters are also typically either hand-tuned or point-estimated and do not capture uncertainty.

In this work, we address SLAM in a generative, probabilistic manner that facilitates the integration of learned components. Inspired by Mirchev et al. [2019], we propose a spatial model that captures free 6-DoF agent movement and simulates the surrounding 3D world. We define our model with the following design goals in mind:

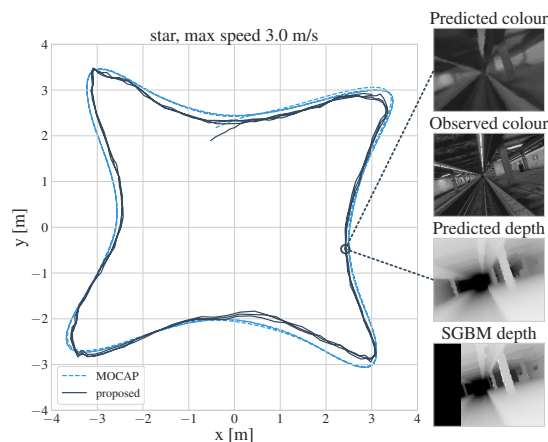


Fig. 1: Example illustration of quadcopter localisation and dense mapping using the proposed method. Left: top-down view of the localisation estimate for a trajectory segment. Right: depth and colour reconstructions from the generative model for one time step.

- 1) End-to-end learning with respect to a single objective.
- 2) Principled treatment of uncertainty in pose and map.
- 3) Expressive predictive distribution suitable for downstream tasks.

The devised method implements agent localisation and dense environment reconstruction with Stochastic Gradient Variational Bayes (SGVB) [Kingma and Welling, 2014] and Bayes by backprop [Blundell et al., 2015]. All variables of interest are inferred as variational posteriors. Furthermore, integrating learned components in the form of neural network amortisations is straightforward, as they are differentiable and comply with the SGD optimisation. To illustrate this, we propose a state-space model of agent dynamics learned from real flight data which we seamlessly include as a prior in the graphical model. We hope that incorporating learning can let us solve more complex, high-level problems that go beyond SLAM in the same framework. We apply the overall model to the Blackbird dataset [Antonini et al., 2018]: real drone flight trajectories with simulated realistic stereo images. The method runs offline and its localisation performance nears that of a state-of-the-art visual inertial odometry (VIO) system.

## II. RELATED WORK

a) *Traditional SLAM*: Listing all prominent examples far outreaches the scope of this work, we therefore refer to [Cadena et al., 2016] for an overview and focus on approaches that share properties with our model. A part of the map variable used in our solution can be interpreted as an occupancy grid map [Moravec and Elfes, 1985, Thrun et al., 2005], using a Gaussian distribution. We note that the map and raycasting models in this work are simple, leaving the discussion of more efficient implementations, e.g. based on octrees like in OctoMap [Hornung et al., 2013], for future work. In KinectFusion [Newcombe et al., 2011a] and DTAM [Newcombe et al., 2011b] a virtual image is formed from a dense map model relative to an initial pose guess, resembling the emission in our generative model. The inferences in this work can be categorised as a method for probabilistic SLAM, other prominent examples of which are FastSLAM [Montemerlo et al., 2002] and RBPF SLAM [Grisetti et al., 2005]. What distinguishes our method is the application of variational inference with SGVB [Kingma and Welling, 2014]. The proposed model does not restrict the used distributions and allows any differentiable functional forms, which enables us to use neural networks.

b) *Spatial generative sequence models*: GTM-SM [Fracaro et al., 2018] focuses on long-term predictions in spatial environments with a non-metric external memory. DDPAE, [Hsieh et al., 2018], SQAIR [Kosiorek et al., 2018] and VTSSI [Akhundov et al., 2019] implement object tracking over time in the deep generative framework. DVBF-LM [Mirchev et al., 2019] is a deep generative model that addresses the tasks of localisation, mapping, navigation and exploration for 2D environments. Our proposed model shares the same probabilistic factorisation as DVBF-LM, but its individual components and approximate posteriors are tailored to real-world 3D modelling.

c) *Integration of learning and SLAM*: The idea of integrating learning with traditional SLAM methods has become more prevalent in recent research. DVSO [Yang et al., 2018] amortises depth estimation with a neural network and successfully incorporates it in DSO [Engel et al., 2018], a well-established visual odometry system. In DeepTAM [Zhou et al., 2018] learning is used to amortise odometry and depth estimation. NeuralSLAM [Zhang et al., 2017] uses learning to amortise writing and reading from a spatial map. CodeSLAM and SceneCode [Bloesch et al., 2018, Zhi et al., 2019] focus on encoding geometric depth readings and semantic information in a low-dimensional latent variable.  $\nabla$ SLAM [Jatavallabhula et al., 2019] explores ways to apply automatic differentiation to traditional engineered SLAM pipelines. Our proposed solution benefits from end-to-end differentiation as well, while putting the main emphasis on deep generative Bayesian modelling.

d) *Variational Bayesian inference for SLAM*: Modern variational inference methods can be used to address the SLAM problem, as illustrated by the following examples. The contribution by Murphy [Murphy, 1999] is one of the first to infer a global matrix-valued map with Bayesian methods. Bayesian

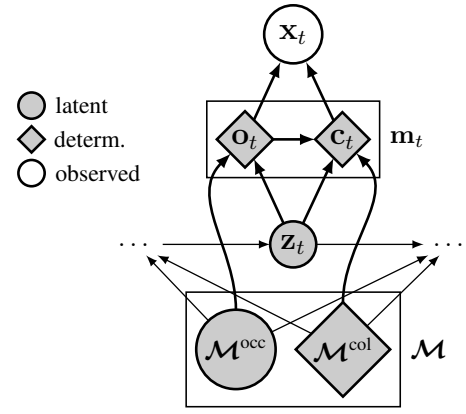


Fig. 2: One time step of the proposed probabilistic graphical model.

Hilbert maps [Senanayake and Ramos, 2017] focus on a fully Bayesian treatment of Hilbert maps for long-term mapping in dynamic environments. In [Fatemi et al., 2015, Lundgren et al., 2015] SLAM for radar data is addressed through traditional variational expectation maximisation. Stochastic variational inference is used to infer agent poses from synthetic data in the work of [Jiang et al., 2019]. DVBF-LM [Mirchev et al., 2019] uses Bayes by backprop [Blundell et al., 2015] for the inference of the global map variable.

## III. METHOD

The model proposed in this work adheres to the graphical model proposed in DVBF-LM [Mirchev et al., 2019], but implements the individual model components differently. In the following, we will first describe the assumed factorisation and then explain the introduced modifications.

### A. Generative Model

The assumed joint distribution of all variables is:

$$\begin{aligned}
 p(\mathbf{x}_{1:T}, \mathbf{z}_{1:T}, \mathbf{m}_{1:T}, \mathcal{M} \mid \mathbf{u}_{1:T-1}) = & \\
 p(\mathcal{M})p(\mathbf{z}_1) & \\
 \prod_{t=1}^T p(\mathbf{x}_t \mid \mathbf{m}_t)p(\mathbf{m}_t \mid \mathbf{z}_t, \mathcal{M}) & \\
 \prod_{t=1}^{T-1} p(\mathbf{z}_{t+1} \mid \mathbf{z}_t, \mathbf{u}_t), & \quad (1)
 \end{aligned}$$

where  $\mathbf{x}_{1:T}$  are observations,  $\mathbf{z}_{1:T}$  agent states,  $\mathbf{m}_{1:T}$  map charts and  $\mathbf{u}_{1:T-1}$  conditional inputs (controls). The factorisation defines a traditional state-space model extended with a global map variable  $\mathcal{M}$ . For a single step  $t$ , an observation  $\mathbf{x}_t$  is generated from a map chart  $\mathbf{m}_t$ —the relevant extract from the global  $\mathcal{M}$  around the current agent pose  $\mathbf{z}_t$  (cf. fig. 2). Chart extraction is given by  $p(\mathbf{m}_t \mid \mathbf{z}_t, \mathcal{M})$ , which can be seen as an attention mechanism. In this graphical model, SLAM is equivalent to inference of the agent states  $\mathbf{z}_{1:T}$  and the map  $\mathcal{M}$ . For the remainder of this work, we assume all observations  $\mathbf{x}_t \in \mathbb{R}^{w \times h \times 4}$  are RGB-D images. Next, we will describe the

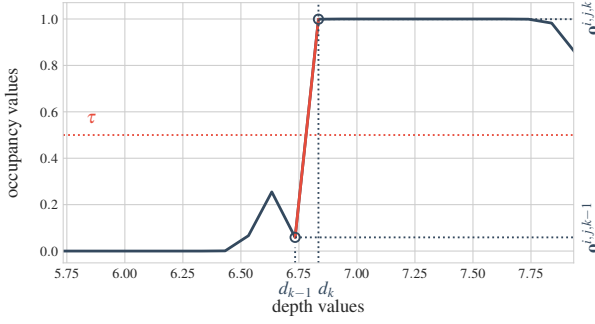


Fig. 3: Linear interpolation during ray casting for a single ray in the emission model.  $d_k$  is the depth corresponding to the first ray value that exceeds  $\tau$ . The output depth  $d$  is formed by linearly interpolating between  $d_{k-1}$  and  $d_k$  based on the occupancy values  $\mathbf{o}^{i,j,k-1}$  and  $\mathbf{o}^{i,j,k}$ .

functional forms of the map  $\mathcal{M}$ , the attention  $p(\mathbf{m}_t | \mathbf{z}_t, \mathcal{M})$ , the emission  $p(\mathbf{x}_t | \mathbf{m}_t)$  and the states  $\mathbf{z}_{1:T}$ .

### B. Geometric Map

The map random variable  $\mathcal{M} = (\mathcal{M}^{\text{occ}}, \mathcal{M}^{\text{col}})$  consists of two components.  $\mathcal{M}^{\text{occ}} \in \mathbb{R}^{l \times m \times n}$  is a spatially arranged 3D grid of scalar cell values that represent occupancy.  $\mathcal{M}^{\text{col}}$  represents the parameters of a feed-forward neural network. The network realises the mapping  $f_{\text{colour}} : \mathbb{R}^3 \rightarrow [0, 255]^3$ , assigning an RGB colour value to each point in space. In this work, the network weights are deterministic and point-estimated online. The respective prior and approximate posterior distributions over the map are:

$$p(\mathcal{M}) = \delta(\mathcal{M}^{\text{col}}) \prod_{i,j,k} \mathcal{N}(\mathcal{M}_{i,j,k}^{\text{occ}} | 0, 1)$$

$$q_{\phi}(\mathcal{M}) = \delta(\mathcal{M}^{\text{col}}) \prod_{i,j,k} \mathcal{N}(\mathcal{M}_{i,j,k}^{\text{occ}} | \mu_{i,j,k}, \sigma_{i,j,k}^2),$$

where  $\delta$  is the Dirac delta function, denoting a point mass density. We assume  $p(\mathcal{M}_{\text{occ}})$  and  $q_{\phi}(\mathcal{M}_{\text{occ}})$  factorise over grid cells. The variational parameters  $\mu_{i,j,k}, \sigma_{i,j,k}$  are optimised with Bayes by backprop [Blundell et al., 2015].

### C. Attention

In the proposed model, the composition of the attention  $p(\mathbf{m}_t | \mathbf{z}_t, \mathcal{M})$  and the emission  $p(\mathbf{x}_t | \mathbf{m}_t)$  implements volumetric ray-casting. We engineer them based on our understanding of geometry [Hartley and Zisserman, 2003] to ensure generalisation across unseen environments.

Following Mirchev et al. [2019], the attention  $p(\mathbf{m}_t | \mathbf{z}_t, \mathcal{M})$  shapes latent charts  $\mathbf{m}_t$ , which correspond to extracts from the map  $\mathcal{M}$  around  $\mathbf{z}_t$ . We identify  $\mathbf{m}_t$  with the part of the map contained in the frustum of the current camera view. To attend to that region, first the intrinsic camera matrix  $\mathbf{K}$  (assumed to be known) and the agent pose  $\mathbf{z}_t$  are used to cast a ray for any pixel  $[i, j]^T$  in the reconstructed observation. The ray is then discretised equidistantly along the depth dimension into  $r$ -many points, resulting into a collection of 3D world coordinates

$\mathbf{p}_t \in \mathbb{R}^{w \times h \times r \times 3}$ . Depth candidate values  $d \in \{k\epsilon\}_{1 \leq k \leq r}$  are associated with each point along a ray, where  $\epsilon$  is a resolution hyperparameter.

The latent chart  $\mathbf{m}_t = (\mathbf{o}_t, \mathbf{c}_t)$  factorises into an occupancy chart  $\mathbf{o}_t \in \mathbb{R}^{w \times h \times r}$  and a colour chart  $\mathbf{c}_t \in \mathbb{R}^{w \times h \times r \times 3}$ . Let  $p_t^{ijk} \in \mathbb{R}^3$  be any 3D point contained in the spanned camera frustum coordinates. To form the occupancy chart  $\mathbf{o}_t$ , cells from the map  $\mathcal{M}^{\text{occ}}$  around  $p_t^{ijk}$  are combined with a weighted kernel

$$o_t^{ijk} = \sum_{l,h,s} \mathcal{M}_{l,h,s}^{\text{occ}} \alpha_{l,h,s}(p^{ijk}).$$

Note that here  $l, h, s$  are indices of the occupancy map voxels. Inspired by Mirchev et al. [2019], we choose a trilinear interpolation kernel for  $\alpha$ . This makes the attention fast and differentiable w.r.t  $\mathbf{z}_t$ . The colour chart  $\mathbf{c}_t = f_{\text{colour}}(\mathbf{p}_t)$  is formed by applying  $f_{\text{colour}}$ , the neural network parameterised through  $\mathcal{M}^{\text{col}}$ , point-wise to each 3D point. In this work, we keep the chart  $\mathbf{m}_t$  deterministic. The full attention procedure can be described as:

$$p(\mathbf{m}_t | \mathbf{z}_t, \mathcal{M}) = \prod_{ijk} \delta(\mathbf{m}_t^{ijk} = f_A(\mathcal{M}, p^{ijk}))$$

$$p^{ijk} = \mathbf{T}(\mathbf{z}_t) \mathbf{K}^{-1} [i, j, 1]^T \underbrace{d}_{:=k\epsilon}.$$

Here  $\mathbf{T}(\mathbf{z}_t) \in \mathbb{SE}(3)$  denotes the rigid camera transformation defined by the current agent state  $\mathbf{z}_t$  and  $i, j, k$  index the points lying inside the attended camera frustum.

### D. Emission Through Ray Casting

The emission model factorises over the observed pixels:

$$p(\mathbf{x}_t | \mathbf{m}_t) = \prod_{ij} p(\mathbf{x}_t^{ij} | \mathbf{m}_t).$$

It operates on the extracted chart  $\mathbf{m}_t = (\mathbf{o}_t, \mathbf{c}_t)$ . Here  $\mathbf{x}_t^{ij} \in \mathbb{R}^4$  denotes an RGB-D pixel value, i.e. for each pixel  $[i, j]^T$  we reconstruct a depth and a colour value:

$$p(\mathbf{x}_t^{ij} | \mathbf{m}_t) = p(d_t^{ij}, \tilde{\mathbf{c}}_t^{ij} | \mathbf{o}_t, \mathbf{c}_t).$$

The mean of the depth value  $d_t^{ij}$  is formed by a function  $f_E$ :

$$f_E(\mathbf{o}_t) = \epsilon \cdot \min_{k \in [r]} k \quad \text{s.t.} \quad \mathbf{o}_t^{ijk} > \tau.$$

$f_E$  traces the ray for pixel  $[i, j]^T$ , searching for the minimum depth  $d = \epsilon k$  for which the occupancy value  $\mathbf{o}_t^{ijk}$  exceeds a threshold  $\tau$  (a hyperparameter).  $\mathbf{o}_t^{ijk}$  is set to 0 for  $k \leq 1$  and  $f_E(\mathbf{o}_t) = r\epsilon$  if no value exceeds  $\tau$  along the ray. Since the above min operation is not differentiable in  $\mathbf{o}_t$ , we linearly interpolate between the depth value for the first ray hit and its predecessor to form the mean (cf. fig. 3):

$$\mu_{d_t}^{ij} = \alpha f_E(\mathbf{o}_t) + (1 - \alpha)(f_E(\mathbf{o}_t) - \epsilon)$$

$$\alpha = \frac{\tau - \mathbf{o}_t^{i,j,k-1}}{\mathbf{o}_t^{i,j,k} - \mathbf{o}_t^{i,j,k-1}}$$

The mean of the emitted colour  $\mu_{\mathbf{c}_t}^{ij} = \mathbf{c}_t^{ijk}$  directly corresponds to the  $k$ -th element of the attended colour values, where  $k$  is the

index of the first hit from raycasting above. A heteroscedastic Laplace distribution is assumed for both the emitted depth and colour values:

$$p(\mathbf{x}_t^{ij} | \mathbf{m}_t) = \text{Laplace}(\mathbf{x}_t^{ij}; (\mu_{d_t}^{ij}, \mu_{c_t}^{ij}), \text{diag}(\sigma_E^{ij})).$$

### E. Agent States

All agent states are represented as vectors  $\mathbf{z}_t = (\boldsymbol{\lambda}_t, \mathbf{o}_t, \mathbf{z}_t^{\text{rest}}) \in \mathbb{R}^{d_z}$ .  $\boldsymbol{\lambda}_t \in \mathbb{R}^3$  is identified with the agent location in space.  $\mathbf{o}_t \in \mathbb{H}^4$  is identified with the agent orientation, represented as a quaternion.  $\mathbf{z}_t^{\text{rest}} \in \mathbb{R}^{d_z-7}$  is a remainder. Depending on the used transition model, it can be identified with  $\dot{\boldsymbol{\lambda}}_t$  alone or it can contain an abstract latent portion not explicitly matching physical quantities.

In [Mirchev et al., 2019] a bootstrap particle filter is used to implement the variational posterior over agent states. The increased model complexity due to the presented raycasting model makes the application of particle filters with sufficiently many particles costly. We therefore opt for a simpler, less expressive variational family that factorises over time:

$$q_\phi(\mathbf{z}_{1:T}) = \prod_t q_\phi(\mathbf{z}_t) = \prod_t \mathcal{N}(\mathbf{z}_t | \boldsymbol{\mu}_t^z, \text{diag}(\boldsymbol{\sigma}_t^z)^2).$$

Here  $\boldsymbol{\mu}_t^z \in \mathbb{R}^{d_z}$  and  $\boldsymbol{\sigma}_t^z \in \mathbb{R}^{d_z}$  are free variables for each latent state and are optimised with SGVB [Kingma and Welling, 2014]. Notably, the above factorisation over individual poses represents a shift in perspective—from filtering towards a method more similar to pose-graph optimisation. One can see the individual terms  $q_\phi(\mathbf{z}_t)$  as the graph nodes, and the loss terms induced by the transition and emission in the objective presented next as the edge constraints.

The portions of the sampled latent states  $\mathbf{o}_t$ , identified with quaternions, are explicitly normalised to unit quaternions after gradient updates before they are used in the rest of the model. This means that the assumed Gaussian distribution is not directly expressed on the manifold  $\mathbb{S}\mathbb{O}(3)$ , but we found that this parameterisation works well enough.

### F. Overall Objective

All of the described elements, together with the transition  $p(\mathbf{z}_t | \mathbf{z}_{t-1}, \mathbf{u}_{t-1})$  which we will discuss in the next section, form the probabilistic graphical model presented in eq. (1). In total, the assumed approximate variational posterior is

$$q_\phi(\mathbf{z}_{1:T})q_\phi(\mathcal{M}) \approx p(\mathbf{z}_{1:T}, \mathcal{M} | \mathbf{x}_{1:T}, \mathbf{u}_{1:T-1}).$$

For the optimisation objective we use the negative *evidence lower bound* (ELBO) [Jordan et al., 1999], given as

$$\begin{aligned} \mathcal{L}_{\text{elbo}} = & -\mathbb{E}_q\left[\sum_{t=1}^T \log p(\mathbf{x}_t | \mathbf{m}_t)\right] \\ & + \text{KL}(q_\phi(\mathcal{M}) || p(\mathcal{M})) \\ & + \mathbb{E}_q\left[\sum_{t=2}^T \text{KL}(q_\phi(\mathbf{z}_t) || p(\mathbf{z}_t | \mathbf{z}_{t-1}, \mathbf{u}_{t-1}))\right]. \quad (2) \end{aligned}$$

We employ the same approximate particle optimisation scheme as in [Mirchev et al., 2019] to deal with long data sequences.

The only optimised parameters are  $\phi$ , containing the variational parameters of the map and the agent states.

### G. Making Image Reconstruction Tractable

Using the full observations during inference is not feasible, as raycasting for all pixels is too computationally demanding. To ensure tractability of the inference method we therefore use reconstruction sampling [Dauphin et al., 2011], emitting a random part of  $\mathbf{x}_t$  at a time, by uniformly selecting  $c$ -many pixel coordinates  $[i, j]^T$  for every gradient step. Here  $c$  is a constant much smaller than the original image size  $wh$ , improving performance by a few orders of magnitude. With this assumption, the model observes all image pixels over the course of training, while also ensuring computations can fit into memory, improving runtime performance and avoiding loss of information due to subsampling or sparse feature selection.

## IV. LEARNING RIGID-BODY DYNAMICS

The proposed spatial model factorisation includes a transition  $p(\mathbf{z}_{t+1} | \mathbf{z}_t, \mathbf{u}_t)$ , which allows for the natural inclusion of priors about the agent movement. This is reflected in the corresponding KL terms in eq. (2), such that the optimisation will have to satisfy both the image reconstruction as well as the movement prior. Note that since we are using variational inference, any differentiable transition model can be integrated as-is, without the need for linearisation.

In this work we propose a framework for learning fully-probabilistic transition models from noisy streams of control inputs and pose observations. We demonstrate how engineering knowledge about the agent dynamics can be exploited by formulating a residual transition. We do not learn the transition with fully-supervised regression. Instead we formulate a generative sequence model for  $T$  time steps. This has two advantages: it allows the separation of aleatoric uncertainty in the observed agent states from epistemic uncertainty in the transition itself, and lets us use an RNN-based approximate posterior over the latent states to tighten the optimised evidence lower bound.

In the following, we assume the agent is equipped with an IMU sensor providing readings  $\ddot{\boldsymbol{\lambda}}_t^{\text{imu}}$  (linear acceleration) and  $\dot{\mathbf{o}}_t^{\text{imu}}$  (angular velocity) over time, which we choose to treat as conditional inputs  $\mathbf{u}_t = (\ddot{\boldsymbol{\lambda}}_t^{\text{imu}}, \dot{\mathbf{o}}_t^{\text{imu}})$ .

### A. Engineering Rigid-Body Dynamics

In the absence of learning, one can use an engineered transition model that integrates the IMU sensor readings using Euler integration. The latent state  $\mathbf{z}_t = (\boldsymbol{\lambda}_t, \mathbf{o}_t, \dot{\boldsymbol{\lambda}}_t)$  then contains the location, orientation and linear velocity of the agent at every time step. The transition is defined as:

$$p(\mathbf{z}_{t+1} | \mathbf{z}_t, \mathbf{u}_t) = \mathcal{N}(\mathbf{z}_{t+1} | f_T(\mathbf{z}_t, \mathbf{u}_t), \text{diag}(\boldsymbol{\sigma}_T)^2).$$

The state update follows the rigid body dynamics

$$f_T(\mathbf{z}_t, \mathbf{u}_t) = \begin{bmatrix} \boldsymbol{\lambda}_{t+1} \\ \mathbf{o}_{t+1} \\ \dot{\boldsymbol{\lambda}}_{t+1} \end{bmatrix} = \begin{bmatrix} \boldsymbol{\lambda}_t + \dot{\boldsymbol{\lambda}}_t \Delta t \\ \mathbf{o}_t \oplus \mathbf{R}(\mathbf{o}_t) \dot{\mathbf{o}}_t^{\text{imu}} \Delta t \\ \dot{\boldsymbol{\lambda}}_t + \mathbf{R}(\mathbf{o}_t) \ddot{\boldsymbol{\lambda}}_t^{\text{imu}} (\Delta t)^2 \end{bmatrix}.$$

Here  $\oplus$  denotes standard quaternion integration. This transition model will serve as a counterpart for the learned model presented next. The standard deviation  $\sigma_T$  is a hyperparameter, estimated via search on the validation set.

### B. Learning a Dynamics Model

In the following, we will describe the proposed framework for learning a dynamics model prior to further forms of spatial reasoning in the full model. The learned transition can then be directly incorporated as a prior in our spatial framework. This should serve as an example for how other model components, such as the attention, emission, map, or newly added functions not discussed in this paper, can be substituted for learned amortisations as well.

We follow the literature on variational state-space models [Fracaro et al., 2016, Karl et al., 2016]. We assume we have a sequence of locations  $\hat{\lambda}_{1:T}$  and orientations  $\hat{o}_{1:T}$  as ground-truth observations, and a sequence of IMU readings, as well as RPM and PWM signals, as conditional inputs:

$$\mathbf{u}_{1:T-1} = (\hat{\lambda}_{1:T-1}^{\text{imu}}, \hat{o}_{1:T-1}^{\text{imu}}, \mathbf{u}_{1:T-1}^{\text{rpm}}, \mathbf{u}_{1:T-1}^{\text{pwm}}).$$

We define the generative state-space model:

$$p(\hat{\lambda}_{1:T}, \hat{o}_{1:T}, \mathbf{z}_{1:T} \mid \mathbf{u}_{1:T-1}) = \delta(\mathbf{z}_1) p(\hat{\lambda}_1, \hat{o}_1 \mid \mathbf{z}_1) \prod_{t=1}^{T-1} p_{\theta_T}(\mathbf{z}_{t+1} \mid \mathbf{z}_t, \mathbf{u}_t) p(\hat{\lambda}_{t+1}, \hat{o}_{t+1} \mid \mathbf{z}_{t+1}).$$

The objective is to learn generative model parameters  $\theta_T$ , such that the marginal likelihood of observed agent poses  $p_{\theta_T}(\hat{\lambda}_{1:T}, \hat{o}_{1:T} \mid \mathbf{u}_{1:T-1})$  is maximised. The latent state is  $\mathbf{z}_t = (\lambda_t, \mathbf{o}_t, \hat{\lambda}_t, \mathbf{z}_t^{\text{rest}})$ , identifying its first three components with location, orientation and linear velocity. The remainder  $\mathbf{z}_t^{\text{rest}}$  acts as an abstract state part. Its role is to absorb any quantities that might affect the transition to the next step, for example higher moments of the agent dynamics or sensor biases accumulated from all previous time steps.

The transition is implemented as a residual feed-forward neural network [He et al., 2016] on top of Euler integration:

$$p_{\theta_T}(\mathbf{z}_{t+1} \mid \mathbf{z}_t, \mathbf{u}_t) = \mathcal{N}(\mathbf{z}_{t+1} \mid \boldsymbol{\mu}_{t+1}, \text{diag}(\boldsymbol{\sigma}_{t+1})^2) \\ \boldsymbol{\mu}_{t+1} = \begin{bmatrix} f_T(\mathbf{z}_t, \mathbf{u}_t) \\ \mathbf{0} \end{bmatrix} + \text{MLP}_{\boldsymbol{\mu}}(\mathbf{z}_t, \mathbf{u}_t) \\ \boldsymbol{\sigma}_{t+1} = \text{MLP}_{\boldsymbol{\sigma}}(\mathbf{z}_t, \mathbf{u}_t),$$

where  $f_T$  is the engineered Euler integration from the previous section and the abstract remainder of the latent state is formed entirely by the network (MLP). This strong inductive bias shapes the transition to resemble regular integration in the beginning of training, while still allowing the MLP to eventually take over and correct biases as necessary.

The emission isolates the location and orientation from the latent state as the means for diagonal Gaussians:

$$p(\hat{\lambda}_t, \hat{o}_t \mid \mathbf{z}_t) = \mathcal{N}(\hat{\lambda}_t, \hat{o}_t \mid (\lambda_t, \mathbf{o}_t), \text{diag}(\boldsymbol{\sigma})^2).$$

The inference over the latent states uses Gaussian fusion as per [Karl et al., 2017], where the necessary inverse emission is given by a bidirectional RNN:

$$\hat{q}(\mathbf{z}_t \mid \hat{\lambda}_{1:T}, \hat{o}_{1:T}, \mathbf{u}_{1:T}) = \mathcal{N}(\mathbf{z}_t \mid \text{RNN}(\hat{\lambda}_{1:T}, \hat{o}_{1:T}, \mathbf{u}_{1:T})).$$

We minimise the negative ELBO w.r.t.  $\theta_T$ :

$$\mathcal{L}(\theta_T) = -\mathbb{E}_q \left[ \sum_{t=1}^T \log p(\hat{\lambda}_t, \hat{o}_t \mid \mathbf{z}_t) \right] \\ + \mathbb{E}_q \left[ \sum_{t=2}^T \text{KL}(q(\mathbf{z}_t) \parallel p_{\theta_T}(\mathbf{z}_t \mid \mathbf{z}_{t-1}, \mathbf{u}_{t-1})) \right],$$

omitting the conditions in  $q$  for brevity.

## V. EXPERIMENTS

The experiments presented next are designed to validate three model aspects—the localisation quality, the usefulness of the reconstructed 3D dense maps and multi-step prediction given future control inputs.

### A. Experimental Setup

For evaluation, we use the Blackbird data set [Antonini et al., 2018]. It consists of over ten hours of real flight data collected from a quadcopter equipped with an IMU sensor. The ground truth locations and orientations are recorded by a motion capture (MOCAP) system. For each trajectory, Blackbird contains realistic simulated stereo images. We obtain depth from these images using OpenCV’s implementation of *Semi-global block matching* (SGBM) [Hirschmuller, 2007] and treat the left RGB camera images and the estimated depth as the observations  $\mathbf{x}_t$ .

We subsample all trajectories to 10 Hz and partition them into a training, validation and test set. The sets contain different trajectories with no overlap. In particular, the test set contains the trajectories *star*, *forward yaw* and *picasso*, *constant yaw*, traversed at different speeds, everything else is used for training and validation. We selected these trajectories in order to compare to the results of [Nisar et al., 2019], which are the only published results on Blackbird at the time of writing. For learning the transition model, we use the training set and we augment the trajectories with random translations in  $\mathbb{R}^3$  and rotations around the  $z$ -axis, to prevent overfitting. The validation set is then used for model selection based on the ELBO value. All model hyperparameters are fixed to the same values for all evaluations. More details can be found in appendices B and C.

### B. Agent Localisation

We evaluate localisation performance of the complete spatial model following Zhang and Scaramuzza [2018]. We report RMSE errors for the agent location and orientation averaged over the whole trajectory (absolute trajectory error, ATE), as well as relative translational RMSE errors for increasingly growing segments.

Figure 4 shows two example localisation estimates for the fastest trajectories in the test set, where the quadcopter flies with

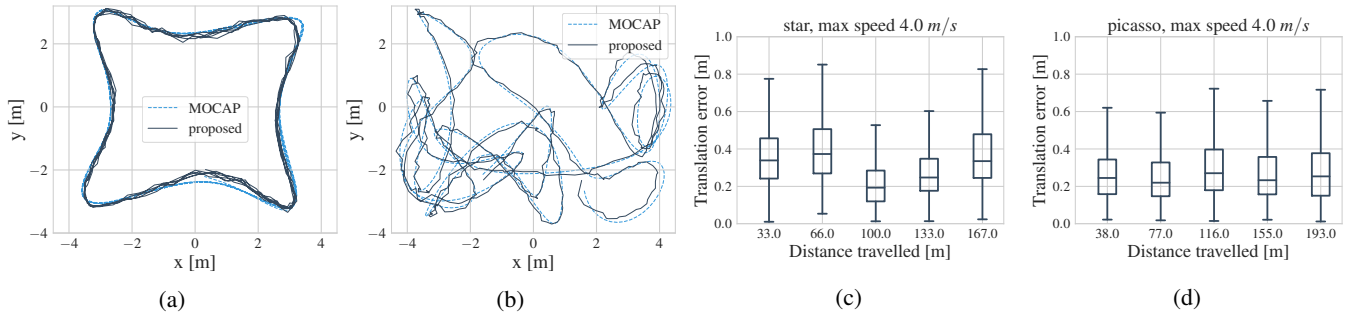


Fig. 4: (a) Top-down view of localisation for *star*, *forward yaw*, *max speed* 4.0m/s. (b) Top-down view of localisation for *picasso*, *constant yaw*, *max speed* 4.0m/s. Only a section of the trajectory is displayed for legibility. (c,d) Aggregated localisation error statistics for all steps up until a given travelled distance ( $x$ -axis) along the *star* and *picasso* trajectories, following the evaluation in [Zhang and Scaramuzza, 2018].

TABLE I: Average localisation RMSE across all test trajectory time steps.

Trajectory	Translational RMSE [m]			
	proposed + eng. trans.	proposed + learn. trans.	VIMO	VINS
picasso 1m/s	0.139	0.143	0.055	0.097
picasso 2m/s	0.136	0.131	0.04	0.043
picasso 3m/s	0.120	0.122	0.043	0.045
picasso 4m/s	0.174	0.368	0.049	0.056
star 1m/s	0.110	0.092	0.088	0.102
star 2m/s	0.163	0.626	0.082	0.133
star 3m/s	0.281	0.187	0.183	0.235
star 4m/s	0.156	0.160	-	-
	Rotational RMSE [rad]			
picasso 1m/s	0.053	0.052	0.013	0.011
picasso 2m/s	0.069	0.064	0.007	0.008
picasso 3m/s	0.073	0.070	0.005	0.005
picasso 4m/s	0.124	0.149	0.009	0.011
star 1m/s	0.045	0.044	0.008	0.008
star 2m/s	0.061	0.157	0.01	0.011
star 3m/s	0.080	0.059	0.015	0.016
star 4m/s	0.065	0.059	-	-

up to 4.0m/s. Over more than 150m the average translational error never exceeds 0.4m (cf. figs. 4c and 4d). The global map variable  $\mathcal{M}$  stabilises localisation and prevents drift from compounding over time. Empirically, we further found that modelling colour significantly helps with *perceptual aliasing* in the environment. In table I we compare the average localisation RMSE of the proposed model over all steps to that of VIMO [Nisar et al., 2019] and VINS-MONO [Qin et al., 2018], two state-of-the-art VIO systems. We carry over the results from [Nisar et al., 2019]. While the localisation estimates of our framework are not as accurate as those of the other two systems, we found that our solution had no difficulty with the fastest *star* test set trajectory, for which both VIO systems have been reported to fail without specifically being tuned for it. It should be noted, however, that both baselines run in real-time, whereas in its current form our method does not.

In terms of the integrated transition  $p(\mathbf{z}_t | \mathbf{z}_{t-1}, \mathbf{u}_{t-1})$ , we find that the learned transition performs on par with its

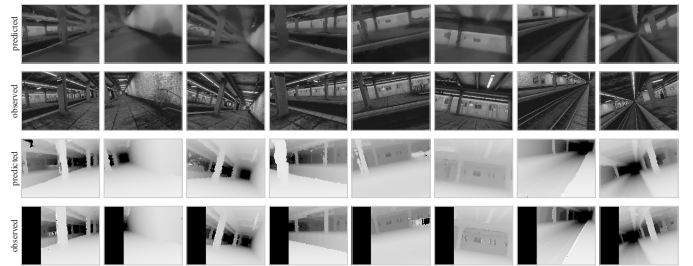


Fig. 5: Emissions at different trajectory points, sampled at a one second interval. From top to bottom: predicted colour, observed colour, predicted depth, observed depth (estimated with SGBM, which does not provide depth estimates for the leftmost part of the images due to parallax).

engineered counterpart when used in the complete model, with the exception of two noticeable outliers—*picasso*, *max speed* 4.0 m/s and *star*, *max speed* 2.0 m/s (cf. table I). On closer examination, we found that this is because of a large localisation error during landing at the end of the trajectories. In both cases the agent fails to land correctly, and in *picasso*, *max speed* 4.0 m/s it falls over. At that point the control inputs to the learned model are out-of-distribution (cf. appendix A), and it fails to generalise to the unseen case.

Overall, localisation is successful for all test trajectories and its accuracy is practical and approaching that of state-of-the-art VIO systems. At the same time, the proposed model is fully-probabilistic and flexible regarding the integration of learned components.

### C. Dense Geometric Mapping

Next we focus on the reconstructed map, obtained as an approximate variational posterior  $q_\phi(\mathcal{M})$ . We take the *NYC subway station* Blackbird environment as an example, in which the test set trajectories take place. Figure 5 shows reconstructions from the generative model along an example trajectory segment. The model can successfully generate both colour and depth based on the approximate map posterior

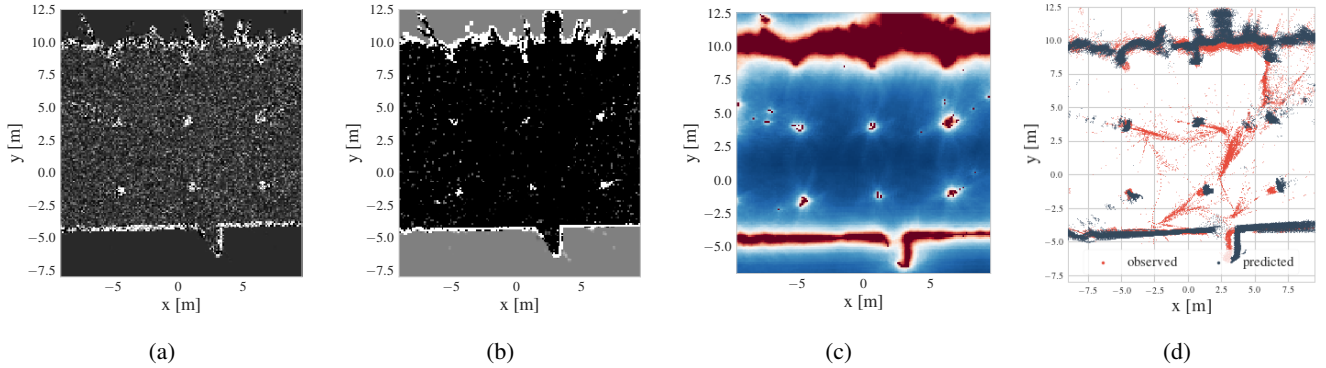


Fig. 6: An example illustration of a reconstructed dense map for the *NYC subway station* environment. Note that columns from the subway are captured in the reconstructed map. (a) Occupancy map uncertainty evaluated along a horizontal slice (white means low uncertainty). (b) Occupancy map mean evaluated along the same horizontal slice (white means occupied). (c) Collision cost-to-go evaluated for all states along the same horizontal slice (red means high cost). (d) Generated point cloud (black, plotted with inferred agent poses) vs. observed point cloud (red, plotted with ground truth MOCAP poses).

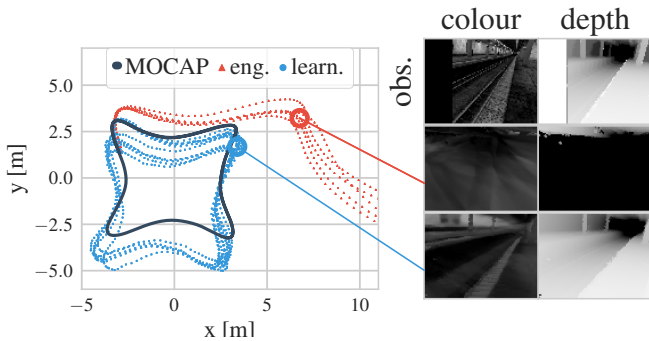


Fig. 7: Generative predictions using the engineered transition vs. the learned transition in the complete spatial model. Left: top-down view of 200-step location predictions. Right: predicted colour and depth for the same step along the predicted trajectory for both models.

$q_\phi(\mathcal{M})$ . Note that the true observations are not needed for this, as all of the information is recorded in  $\mathcal{M}^{\text{occ}}$  and  $\mathcal{M}^{\text{colour}}$  through gradient descent. Even though we use reconstruction sampling during training, on average all image pixels contribute to learning the map. This leads to dense predictions generated by the emission model. The inferred map correctly filters out wrong observations, as can be seen in the top-down point-cloud comparison in fig. 6d, noting the subway station columns.

#### D. Using Maps for Downstream Tasks

Besides serving as an anchor to prevent drift during localisation, a map estimate can also be used to define downstream navigation and exploration tasks. Since the map is modelled as a random variable, the approximate posterior  $q_\phi(\mathcal{M})$  also gives us an uncertainty estimate, in this work only applying to  $\mathcal{M}^{\text{occ}}$ . Figure 6a shows an example horizontal slice from the occupancy grid, along which the map uncertainty is evaluated. The uncertainty is lowest inside the space contained between the subway station walls, and high on the outside where the

agent has not visited. Meaningful map uncertainty is useful, as it can be used for information-theoretic exploration [Mirchev et al., 2019].

The dense map can also be used to construct navigation plans. We show this by computing a cost-to-go:

$$J(\mathbf{z}_1) = \mathbb{E}_{\mathbf{u}_{1:T}, \mathbf{z}_{1:T} \sim p(\cdot)} \left[ \sum_{t=1}^T c(\mathbf{u}_t, \mathbf{z}_t) \right]$$

for a horizon of  $T = 40$  steps [Bertsekas, 2005]. The cost  $c(\mathbf{u}, \mathbf{z})$  is the occupancy value in the map at the location given by  $\mathbf{z}$ , essentially giving a collision cost. To simulate a control policy, we use an empirical distribution of randomly picked 40-step sequences of IMU readings from the test dataset, which we use as  $\mathbf{u}_{1:T}$ . Then we generatively sample future states  $\mathbf{z}_{1:T}$  for these controls and evaluate the respective costs. Figure 6c shows  $J(\mathbf{z})$  evaluated for all states along the considered 2D slice of the map. The collision cost is high near the walls and columns, and gradually drops off in the free space of the environment.

#### E. Generating Future Predictions

The proposed generative model lets us predict the agent movement and observations for a sequence of future conditional inputs, i.e.  $p(\mathbf{z}_{2:T}, \mathbf{x}_{1:T} \mid \mathbf{u}_{1:T-1}, \mathbf{z}_1)$ . The fidelity of these predictions is crucial for model-based planning and decision-making. Figure 7 shows a representative example for predictive performance of the full spatial model for 200 steps in the future, comparing both the engineered and learned transition priors. Long-term prediction is significantly better when the learned model is used, indicating that it corrects biases present in the agent sensors. Conversely, with the engineered transition localisation drift is higher and wrong map regions are queried for generation, translating into wrong depth and colour images being predicted.

Evaluated on 200 test set trajectories of length 100, the learned transition model significantly outperforms the engineered IMU integration, with an average translational RMSE

of 1.156 and rotational RMSE of 0.096, compared to 13.768 and 0.111 for the engineered model. Similarly, the pixel-wise log-likelihood of the observation predictions is  $-1.23$  when the learned model is used, and  $-1.85$  for the engineered model, averaged over 1000 images. This evaluation clearly illustrates the positive effect of integrating learned components in the proposed generative framework.

## VI. CONCLUSION

This work is the first to show that dense 3D mapping and 6-DoF localisation can be accomplished in a deep generative probabilistic framework using variational inference. The proposed spatial model is fully-differentiable and can be optimised with SGD. We further propose a probabilistic method for learning agent dynamics from prerecorded data. We demonstrate that deep priors can be integrated with ease in the overall spatial solution, using the learned transition as an example, which significantly boosts predictive performance. The proposed framework was used to model quadcopter flight data, exhibiting performance approaching that of a state-of-the-art VIO system and bearing promise for real-world applications. In the future, we would like to address the current model's speed limitations and move towards reasoning about spatial aspects that go beyond SLAM in the same framework.

## REFERENCES

- Martín Abadi, Paul Barham, Jianmin Chen, Zhifeng Chen, Andy Davis, Jeffrey Dean, Matthieu Devin, Sanjay Ghemawat, Geoffrey Irving, Michael Isard, et al. Tensorflow: A system for large-scale machine learning. In *12th {USENIX} Symposium on Operating Systems Design and Implementation ({OSDI} 16)*, pages 265–283, 2016.
- Adnan Akhundov, Maximilian Soelch, Justin Bayer, and Patrick van der Smagt. Variational tracking and prediction with generative disentangled state-space models. *arXiv preprint arXiv:1910.06205*, 2019.
- Amado Antonini, Winter Guerra, Varun Murali, Thomas Sayre-McCord, and Sertac Karaman. The blackbird dataset: A large-scale dataset for uav perception in aggressive flight. In *2018 International Symposium on Experimental Robotics (ISER)*, 2018.
- Herbert Bay, Tinne Tuytelaars, and Luc Van Gool. Surf: Speeded up robust features. In *European conference on computer vision*, pages 404–417. Springer, 2006.
- Dimitri P. Bertsekas. *Dynamic Programming and Optimal Control*, volume I. Athena Scientific, Belmont, MA, USA, 3rd edition, 2005.
- Michael Bloesch, Jan Czarnowski, Ronald Clark, Stefan Leutenegger, and Andrew J. Davison. Codeslam - learning a compact, optimisable representation for dense visual slam. *2018 IEEE/CVF Conference on Computer Vision and Pattern Recognition*, pages 2560–2568, 2018.
- Charles Blundell, Julien Cornebise, Koray Kavukcuoglu, and Daan Wierstra. Weight uncertainty in neural networks. *CoRR*, abs/1505.05424, 2015. URL <http://arxiv.org/abs/1505.05424>.
- Cesar Cadena, Luca Carlone, Henry Carrillo, Yasir Latif, Davide Scaramuzza, José Neira, Ian D. Reid, and John J. Leonard. Past, present, and future of simultaneous localization and mapping: Toward the robust-perception age. *IEEE Trans. Robotics*, 32(6):1309–1332, 2016. doi: 10.1109/TRO.2016.2624754. URL <https://doi.org/10.1109/TRO.2016.2624754>.
- Yann N. Dauphin, Xavier Glorot, and Yoshua Bengio. Large-scale learning of embeddings with reconstruction sampling. In *Proceedings of the 28th International Conference on Machine Learning, ICML 2011, Bellevue, Washington, USA, June 28 - July 2, 2011*, pages 945–952, 2011. URL [https://icml.cc/2011/papers/491\\_icmlpaper.pdf](https://icml.cc/2011/papers/491_icmlpaper.pdf).
- Hugh Durrant-Whyte, David Rye, and Eduardo Nebot. Localization of autonomous guided vehicles. In Georges Giralt and Gerhard Hirzinger, editors, *Robotics Research*, pages 613–625, London, 1996. Springer London. ISBN 978-1-4471-0765-1.
- J. Engel, V. Koltun, and D. Cremers. Direct sparse odometry. *IEEE Transactions on Pattern Analysis and Machine Intelligence*, March 2018.
- Maryam Fatemi, Lennart Svensson, Lars Hammarstrand, and Malin Lundgren. Variational bayesian em for slam. In *2015 IEEE 6th International Workshop on Computational Advances in Multi-Sensor Adaptive Processing (CAMSAP)*, pages 501–504. IEEE, 2015.
- Christian Forster, Matia Pizzoli, and Davide Scaramuzza. Svo: Fast semi-direct monocular visual odometry. In *2014 IEEE international conference on robotics and automation (ICRA)*, pages 15–22. IEEE, 2014.
- Marco Fraccaro, Søren Kaae Sønderby, Ulrich Paquet, and Ole Winther. Sequential neural models with stochastic layers. In *Advances in Neural Information Processing Systems 29: Annual Conference on Neural Information Processing Systems 2016, December 5-10, 2016, Barcelona, Spain*, pages 2199–2207, 2016.
- Marco Fraccaro, Danilo Jimenez Rezende, Yori Zwols, Alexander Pritzel, S. M. Ali Eslami, and Fabio Viola. Generative temporal models with spatial memory for partially observed environments. *CoRR*, abs/1804.09401, 2018. URL <http://arxiv.org/abs/1804.09401>.
- Dorian Gálvez-López and J. D. Tardós. Bags of binary words for fast place recognition in image sequences. *IEEE Transactions on Robotics*, 28(5):1188–1197, October 2012. ISSN 1552-3098. doi: 10.1109/TRO.2012.2197158.
- Giorgio Grisetti, Cyrill Stachniss, and Wolfram Burgard. Improving grid-based slam with rao-blackwellized particle filters by adaptive proposals and selective resampling. *Proceedings of the 2005 IEEE International Conference on Robotics and Automation*, pages 2432–2437, 2005.
- Richard Hartley and Andrew Zisserman. *Multiple view geometry in computer vision*. Cambridge university press, 2003.
- Kaiming He, Xiangyu Zhang, Shaoqing Ren, and Jian Sun. Deep residual learning for image recognition. In *Proceedings of the IEEE conference on computer vision and pattern*



- recognition, pages 770–778, 2016.
- Heiko Hirschmuller. Stereo processing by semiglobal matching and mutual information. *IEEE Transactions on pattern analysis and machine intelligence*, 30(2):328–341, 2007.
- Armin Hornung, Kai M. Wurm, Maren Bennewitz, Cyrill Stachniss, and Wolfram Burgard. OctoMap: An efficient probabilistic 3D mapping framework based on octrees. *Autonomous Robots*, 2013. doi: 10.1007/s10514-012-9321-0. URL <http://octomap.github.com>. Software available at <http://octomap.github.com>.
- Jun-Ting Hsieh, Bingbin Liu, De-An Huang, Fei-Fei Li, and Juan Carlos Niebles. Learning to decompose and disentangle representations for video prediction. In *Advances in Neural Information Processing Systems 31: Annual Conference on Neural Information Processing Systems 2018, NeurIPS 2018, 3-8 December 2018, Montréal, Canada*, pages 515–524, 2018.
- Krishna Murthy Jatavallabhula, Ganesh Iyer, and Liam Paull. gradslam: Dense slam meets automatic differentiation, 2019.
- Xiaoyue Jiang, Hang Yu, Michael Hoy, and Justin Dauwels. Robust linear-complexity approach to full slam problems: Stochastic variational bayes inference. In *2019 IEEE 90th Vehicular Technology Conference (VTC2019-Fall)*, pages 1–5. IEEE, 2019.
- Michael I Jordan, Zoubin Ghahramani, Tommi S Jaakkola, and Lawrence K Saul. An introduction to variational methods for graphical models. *Machine learning*, 37(2):183–233, 1999.
- Maximilian Karl, Maximilian Sölch, Justin Bayer, and Patrick van der Smagt. Deep variational bayes filters: Unsupervised learning of state space models from raw data. *CoRR*, abs/1605.06432, 2016. URL <http://arxiv.org/abs/1605.06432>.
- Maximilian Karl, Maximilian Soelch, Philip Becker-Ehmck, Djalel Benbouzid, Patrick van der Smagt, and Justin Bayer. Unsupervised real-time control through variational empowerment. *arXiv preprint arXiv:1710.05101*, 2017.
- Diederik P. Kingma and Jimmy Ba. Adam: A method for stochastic optimization. *CoRR*, abs/1412.6980, 2014. URL <http://arxiv.org/abs/1412.6980>.
- Diederik P Kingma and Max Welling. Auto-encoding variational bayes. In *Proceedings of the 2nd International Conference on Learning Representations (ICLR)*, 2014.
- Daphne Koller and Nir Friedman. *Probabilistic Graphical Models - Principles and Techniques*. MIT Press, 2009. ISBN 978-0-262-01319-2. URL <http://mitpress.mit.edu/catalog/item/default.asp?tttype=2&tid=11886>.
- Adam Kosiorek, Hyunjik Kim, Yee Whye Teh, and Ingmar Posner. Sequential attend, infer, repeat: Generative modelling of moving objects. In S. Bengio, H. Wallach, H. Larochelle, K. Grauman, N. Cesa-Bianchi, and R. Garnett, editors, *Advances in Neural Information Processing Systems 31*, pages 8606–8616. Curran Associates, Inc., 2018.
- D. G. Lowe. Object recognition from local scale-invariant features. In *Proceedings of the Seventh IEEE International Conference on Computer Vision*, volume 2, pages 1150–1157 vol.2, Sep. 1999. doi: 10.1109/ICCV.1999.790410.
- Malin Lundgren, Lennart Svensson, and Lars Hammarstrand. Variational bayesian expectation maximization for radar map estimation. *IEEE Transactions on Signal Processing*, 64(6): 1391–1404, 2015.
- Atanas Mirchev, Baris Kayalibay, Maximilian Soelch, Patrick van der Smagt, and Justin Bayer. Approximate bayesian inference in spatial environments. In *Proceedings of Robotics: Science and Systems*, Freiburg/Breisgau, Germany, June 2019. doi: 10.15607/RSS.2019.XV.083.
- Michael Montemerlo, Sebastian Thrun, Daphne Koller, and Ben Wegbreit. Fastslam: A factored solution to the simultaneous localization and mapping problem. In *AAAI/IAAI*, 2002.
- Hans Moravec and Alberto Elfes. High resolution maps from wide angle sonar. In *Proceedings. 1985 IEEE International Conference on Robotics and Automation*, volume 2, pages 116–121. IEEE, 1985.
- Raul Mur-Artal and Juan D Tardós. Orb-slam2: An open-source slam system for monocular, stereo, and rgb-d cameras. *IEEE Transactions on Robotics*, 33(5):1255–1262, 2017.
- Kevin P. Murphy. Bayesian map learning in dynamic environments. In *Advances in Neural Information Processing Systems 12, [NIPS Conference, Denver, Colorado, USA, November 29 - December 4, 1999]*, pages 1015–1021, 1999.
- Richard A. Newcombe, Shahram Izadi, Otmar Hilliges, David Molyneaux, David Kim, Andrew J. Davison, Pushmeet Kohli, Jamie Shotton, Steve Hodges, and Andrew W. Fitzgibbon. Kinectfusion: Real-time dense surface mapping and tracking. *2011 10th IEEE International Symposium on Mixed and Augmented Reality*, pages 127–136, 2011a.
- Richard A. Newcombe, Steven Lovegrove, and Andrew J. Davison. Dtam: Dense tracking and mapping in real-time. *2011 International Conference on Computer Vision*, pages 2320–2327, 2011b.
- Barza Nisar, Philipp Foehn, Davide Falanga, and Davide Scaramuzza. Vimo: Simultaneous visual inertial model-based odometry and force estimation. In *Proceedings of Robotics: Science and Systems*, Freiburg/Breisgau, Germany, June 2019. doi: 10.15607/RSS.2019.XV.082.
- Tong Qin, Peiliang Li, and Shaojie Shen. Vins-mono: A robust and versatile monocular visual-inertial state estimator. *IEEE Transactions on Robotics*, 34(4):1004–1020, 2018.
- E. Rublee, V. Rabaud, K. Konolige, and G. Bradski. Orb: An efficient alternative to sift or surf. In *2011 International Conference on Computer Vision*, pages 2564–2571, Nov 2011. doi: 10.1109/ICCV.2011.6126544.
- Ransalu Senanayake and Fabio Ramos. Bayesian hilbert maps for dynamic continuous occupancy mapping. In Sergey Levine, Vincent Vanhoucke, and Ken Goldberg, editors, *Proceedings of the 1st Annual Conference on Robot Learning*, volume 78 of *Proceedings of Machine Learning Research*, pages 458–471. PMLR, 13–15 Nov 2017. URL <http://proceedings.mlr.press/v78/senanayake17a.html>.
- Sebastian Thrun, Wolfram Burgard, and Dieter Fox. *Probabilistic Robotics (Intelligent Robotics and Autonomous Agents)*. The MIT Press, 2005. ISBN 0262201623.
- Dustin Tran, Matthew D. Hoffman, Dave Moore, Christopher Suter, Srinivas Vasudevan, Alexey Radul, Matthew Johnson,

- and Rif A. Saurous. Simple, distributed, and accelerated probabilistic programming. In *Neural Information Processing Systems*, 2018.
- Bill Triggs, Philip F McLauchlan, Richard I Hartley, and Andrew W Fitzgibbon. Bundle adjustment—a modern synthesis. In *International workshop on vision algorithms*, pages 298–372. Springer, 1999.
- N. Yang, R. Wang, J. Stueckler, and D. Cremers. Deep virtual stereo odometry: Leveraging deep depth prediction for monocular direct sparse odometry. In *eccv*, September 2018.
- Jingwei Zhang, Lei Tai, Joschka Boedecker, Wolfram Burgard, and Ming Liu. Neural slam: Learning to explore with external memory. *arXiv preprint arXiv:1706.09520*, 2017.
- Zichao Zhang and Davide Scaramuzza. A tutorial on quantitative trajectory evaluation for visual(-inertial) odometry. In *IEEE/RSJ Int. Conf. Intell. Robot. Syst. (IROS)*, 2018.
- Shuaifeng Zhi, Michael Bloesch, Stefan Leutenegger, and Andrew J Davison. Scenecode: Monocular dense semantic reconstruction using learned encoded scene representations. In *Proceedings of the IEEE Conference on Computer Vision and Pattern Recognition*, pages 11776–11785, 2019.
- H. Zhou, B. Ummenhofer, and T. Brox. Deeptam: Deep tracking and mapping. In *European Conference on Computer Vision (ECCV)*, 2018. URL <http://lmb.informatik.uni-freiburg.de/Publications/2018/ZUB18>.

APPENDIX A  
CASE STUDY: DRONE LANDING

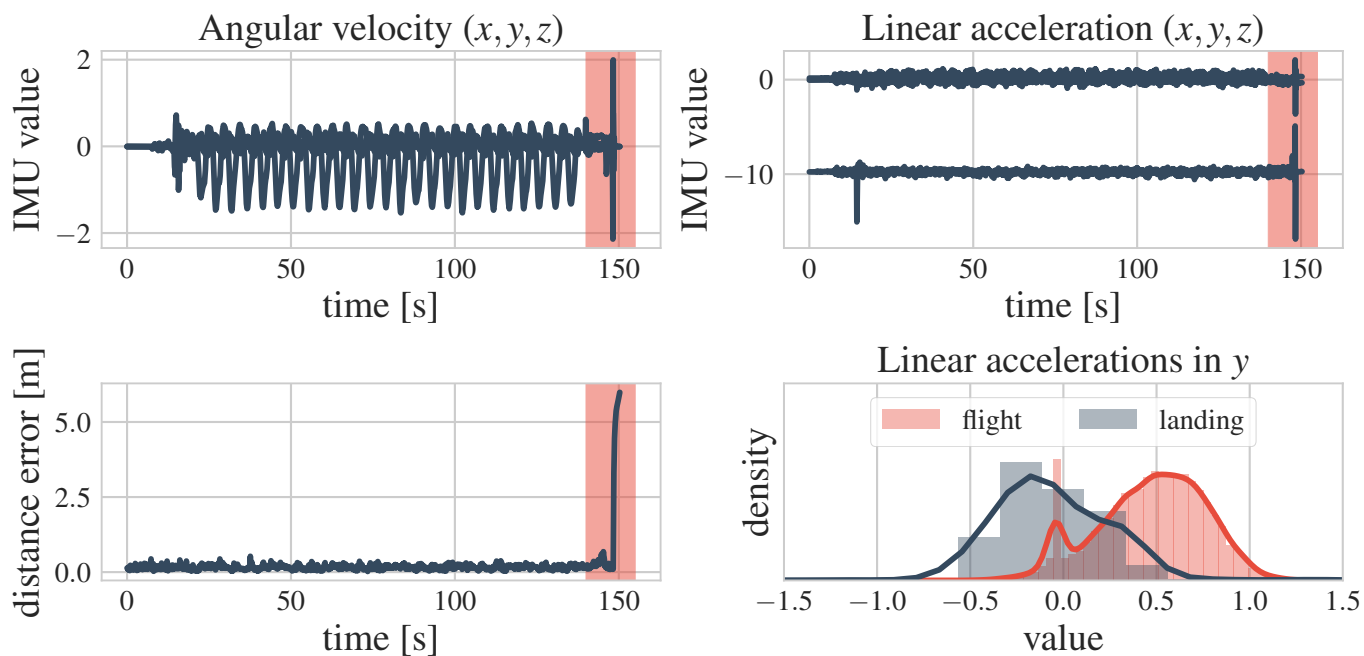


Fig. 8: Illustration of the discussed failure landing of the quadcopter at the end of the two test set trajectories, taking *star, max speed 2.0 m/s* as an example. The problematic segment of the trajectory is marked with a red vertical band. Note the outlier controls at the end. Top left: angular velocity IMU readings. Top right: linear acceleration IMU readings. Bottom left: absolute Euclidean distance error w.r.t. the ground truth MOCAP locations. Note how the error is large only at the end of the trajectory, and directly coincides with the outlier controls. Bottom right: comparison of the distribution of linear accelerations in  $y$  during flight (red) vs. during landing (gray). The controls during landing are out of distribution for the learned transition model.

## APPENDIX B

### DATA DETAILS AND OVERALL SETUP

For all presented experiments we used the Blackbird data set [Antonini et al., 2018], which can be found here: <https://github.com/mit-fast/Blackbird-Dataset>. In the following we describe the exact pre-processing of the data.

#### A. Data Partitioning and Usage

The data was partitioned into a training, a validation and a test set. The trajectory shapes (e.g. *star*, *picasso*, *patrick*, etc.) in every split were different. This was done to prevent accidental overfitting of the learned transition model to any particular trajectory shape. You can refer to appendix F for the exact trajectories used for each split, along with the number of steps in each trajectory after pre-processing (which includes subsampling).

The training set was used only to train the learned transition model  $p_{\theta_T}(\mathbf{z}_{t+1} | \mathbf{z}_t, \mathbf{u}_t)$ , following the method described in section IV. The learned transition model is trained separately before it is used as a prior in the full spatial model. Pretraining the model on multiple trajectories beforehand, as opposed to training it from scratch during SLAM inference, ensures that the transition really captures the agent dynamics and does not overfit the currently explored environment. The training trajectories were further randomly rotated around the  $z$  axis and linearly translated in space.

The validation set was used for checkpointing and selecting the best weights  $\theta_T$  of the neural network in the learned transition model, based on the ELBO defined in section IV. The validation set was also used for hyperparameter selection for the engineered transition model, the learned transition model and the full spatial model. The best hyperparameters for all models (cf. appendix C) were selected with random search. You can find details for the search ranges in appendix D.

The test set was used for evaluation only—all results reported in the experimental section of the paper were done on the test data. The full spatial model was tested with the forward yaw *star* trajectories, speeds 1.0 m/s to 4.0 m/s and with the constant yaw *picasso* trajectories, speeds 1.0 m/s to 4.0 m/s, to match the evaluation in [Nisar et al., 2019]. These trajectories take place in the *NYC subway station* environment.

#### B. Data Preprocessing

Each trajectory contains IMU, RPM and PWM readings, MOCAP ground truth pose observations, as well as simulated grayscale images from a forward-facing stereo pair and a downward-facing camera.

We pre-processed every trajectory in the following way:

- Ground truth MOCAP state readings were extracted from the provided ROS bags.
- Downward-facing images were ignored.
- The remaining data was subsampled to 10 Hz, using nearest neighbour subsampling based on the provided time stamps.
- Depth was then precomputed from the left and right images using OpenCV’s SGBM [Hirschmuller, 2007].

- For every time step, the right colour image was then ignored, while the left image and the depth estimate were together treated as an RGB-D observation  $\mathbf{x}_t \in \mathbb{R}^{w \times h \times 4}$ .
- The provided IMU readings are measured in the coordinate frame of the IMU sensor. Therefore, they had to be rotated to the body frame of the agent, using the respective quaternion provided with the data set:  $\mathbf{q} = [0.707, 0.005, -0.004, 0.706]^T$ .

The intrinsic parameters of the camera, specifying the intrinsic camera matrix  $\mathbf{K}$ , and the stereo baseline were fixed to the values provided with the data set:

- Stereo baseline: 0.1m.
- Image size:  $1024 \times 768$ .
- Focal length, x: 665.1.
- Focal length, y: 665.1.
- Principal point offset, x: 511.5.
- Principal point offset, y: 383.5.

Depth was computed based on the disparity values produced by SGBM. We used the following parameters, keeping the default values for everything else:

- Block size: 5.
- Min. disparity: 0.
- Max. disparity: 256.

We did not filter the images and the produced depth values in any way and treated them as direct observations, to limit the pre-processing steps as much as possible and rely on the defined spatial model instead. Note that due to the simplicity of the method used for depth estimation, the depth observations contain significant amounts of noise (e.g. fig. 6d). The pixel values for the color images were normalized to be in the range  $[0, 1]$ .

## APPENDIX C MODEL DETAILS

This section lists all model and optimisation hyperparameters used for generating the results reported in the paper.

#### A. Full Spatial Model

The full spatial model uses either the engineered or the learned transition, see section C-C and section C-B for their respective hyperparameters.

1) *Optimisation*: After subsampling, the trajectories in the Blackbird dataset can still contain thousands of time steps. To deal with this, during inference the proposed model follows the approximate particle optimisation scheme introduced in [Mirchev et al., 2019], using chunks of 5 time steps for every gradient update, using 50 approximating state particles and applying the respective particle updates after every gradient step.

Adam [Kingma and Ba, 2014] is used to optimise the parameters  $\phi$  for the approximate posterior distribution  $q_{\phi}(\mathbf{z}_{1:T}, \mathcal{M})$ . Table II lists the used optimiser hyperparameters. Note that due to the employed attention  $p(\mathbf{m}_t | \mathbf{z}_t, \mathcal{M})$ , due to the reconstruction sampling in the emission and due to the approximate optimisation scheme mentioned above (which

uses only a chunk of the trajectory at a time), only a part of the parameters for the occupancy map and the full trajectory of agent states is used for a gradient step. In other words, gradient updates happen locally in the spatially arranged occupancy map parameters, based on the currently selected local chunk of the agent trajectory. Because of this, momentum is disabled in Adam for both the occupancy map and the agent states, to avoid accidental drift in regions currently not covered by the optimisation.

For every variable in question, the same optimiser is used to optimise the mean and scale of the assumed distribution (where applicable). For any scale distribution parameters (e.g. standard deviations for the assumed Gaussian distributions), the optimisation is performed in log-space to satisfy the positive value constraint.

TABLE II: Optimisation hyperparameters for the full spatial model.

Variables	Parameter	Value
$\mathbf{z}_{1:T}$	Adam, learning rate	0.001
	Adam, $\beta_1$	0.0
	Adam, $\beta_2$	0.999
$\mathcal{M}^{occ}$	Adam, learning rate	0.05
	Adam, $\beta_1$	0.0
	Adam, $\beta_2$	0.999
$\mathcal{M}^{col}$	Adam, learning rate	0.001
	Adam, $\beta_1$	0.9
	Adam, $\beta_2$	0.999

2) *Initialisation of new poses*: While performing SLAM, data is added incrementally to the spatial model, to emulate online usage of the method. A new time step  $t$  is explored every 500 gradient steps, effectively adding a new observation  $\mathbf{x}_t$  and a new conditional input  $\mathbf{u}_t$  to the data. Whenever a new time step is added, the parameters of the corresponding state  $\mathbf{z}_t$  are unlocked for optimisation and initialized according to table III.

3) *Component Parameters*: The rest of the hyperparameters for the full spatial model, including initial values for the optimised variational parameters, are specific to the individual model components and are listed in table III.

The scale  $\sigma_E$  for the heteroscedastic Laplace emission  $p(\mathbf{x}_t | \mathbf{m}_t)$  is learned with gradient descent (applied in log-space). The colour part of  $\sigma_E$  is forced to be 10 times smaller than that for the depth part, to account for the different scales of the observed values (colour range is  $[0, 1]$ , depth range is  $[0, 20]$ ).

### B. Learned Transition

The learned transition is obtained by training the generative parameters  $\theta_T$  in the context of the model defined in section IV. When reconstructing orientations in that model, we do not reconstruct quaternions directly because of the ambiguity  $\mathbf{q} = -\mathbf{q}$ . Instead we reconstruct the rotation matrix corresponding to the observed orientation  $\hat{\mathbf{o}}_t$ , i.e. the mean of the emission  $p(\hat{\mathbf{o}}_t | \mathbf{z}_t)$  is a rotation matrix constructed from the quaternion  $\mathbf{o}_t$  that's part of the latent state  $\mathbf{z}_t$ . When used in the full spatial

TABLE III: Hyperparameters of the individual spatial model components.

Component	Parameter	value
$\mathbf{z}_t$	init. value for $\mu_t$	$\mu_{t-1}$
	init. value for $\sigma_t$	$0.01 \times \mathbf{1}$
$\mathcal{M}^{occ}$	grid size	$200 \times 200 \times 200$
	init. value for $\mu_{i,j,k}$	-0.5
	init. value for $\sigma_{i,j,k}$	0.1
$\mathcal{M}^{col}$	# hidden layers	5
	# hidden units	256
	activation	softsign
	residual connections	true
$p(\mathbf{m}_t   \mathbf{z}_t, \mathcal{M})$	$\epsilon$ (ray resolution)	0.1m
	max depth ( $k\epsilon$ )	20m
	# reconstr. pixels	200

TABLE IV: Hyperparameters of the learned transition model.

Component	Parameter	value
$p_{\theta_T}(\mathbf{z}_{t+1}   \mathbf{z}_t, \mathbf{u}_t)$	# hidden layers	5
	# hidden units	64
	activation	relu
	residual connections	true
	size of $\mathbf{z}^{rest}$	8
$\hat{q}(\mathbf{z}_t   \hat{\lambda}_{1:T}, \hat{\mathbf{o}}_{1:T}, \mathbf{u}_{1:T})$	RNN type	LSTM
	# RNN units	64

model, the weights of the transition neural network  $\theta_T$  are fixed to their pretrained values. This is done to avoid accidental overfitting of the transition parameters to the current trajectory and current environment for which SLAM is performed.

The selected hyperparameters of the learned transition are listed in table IV.

### C. Engineered Transition

The gravitational force  $\mathbf{g}$  is subtracted from the IMU readings when applying the Euler integration given by  $f_T$ . The time delta for the integration is set to  $\Delta t = 0.1$ , to match the 10Hz data subsampling. Additionally,  $\sigma_T$  (the diagonal for the assumed Gaussian) was selected based on a hyperparameter search using the validation set. Its diagonal entries are 0.01 for the location state dimensions, 0.001 for the orientation state dimensions and 0.001 for the velocity state dimensions.

## APPENDIX D

### HYPERPARAMETER SEARCH AND EXECUTION DETAILS

All models are implemented in the TensorFlow framework [Abadi et al., 2016], making use of automatic differentiation to optimise model parameters. All probabilistic modelling aspects were implemented using Edward [Tran et al., 2018]. Hyperparameter search (HPS) experiments were executed in a cluster with 8 Tesla V100 GPUs and 40 Intel Xeon E5-2698 CPU cores. Because of the large amount of Blackbird data (4.7 TB) and the current model's speed limitations, the search was performed for a subset of all possible hyperparameters. The performed model selection is therefore not exhaustive, possibly leaving potential for improvement. In the following we list the

considered hyperparameter search ranges and the number of trials for each model.

#### A. HPS: Full Spatial Model

The hyperparameters for the full spatial model were selected based on localisation RMSE for 500-step segments of trajectories in the validation set. A total of 200 experiments were conducted, randomly picking a trajectory segment on which SLAM inference is performed. The considered parameter ranges are listed in table V.

TABLE V: HPS ranges for the full spatial model.

parameter	range
reconstr. pixel count	[100, 200, 500]
$q(\mathcal{M}^{occ})$ init. value stddev	[0.01, 0.1, 1.0]
$p(\mathcal{M}^{occ})$ stddev	[0.1, 1.0, 10.0]
$\mathcal{M}^{occ}$ grid side	[50, 100, 200]
$\mathcal{M}^{occ}$ learning rate	[0.01, 0.05, 0.001]
$\mathcal{M}^{col}$ learning rate	[0.01, 0.05, 0.001]
$\mathbf{z}_{1:T}$ learning rate	[0.01, 0.05, 0.001]

#### B. HPS: Learned Transition Model

The learned transition hyperparameters were selected based on the validation set ELBO value from the model discussed in section IV. A total of 400 experiments were conducted, using all of the blackbird training and validation data. The considered parameter ranges are listed in table VI.

TABLE VI: HPS ranges for the learned transition model.

parameter	range
learning rate	[0.0001, 0.0005, 0.001, 0.005]
$\mathbf{z}^{\text{rest}}$	[8, 16]
# hidden units	[32, 64, 128, 256]
# layers	[2, 3, 4, 5]
activation	[softsign, relu]
# RNN units	[32, 64, 128, 256]

#### C. HPS: Engineered Transition Model

The engineered transition hyperparameters were selected in the same HPS for the full model discussed above, based on localisation RMSE for 500-step segments of trajectories in the validation set. The considered parameter ranges are listed in table VII.

TABLE VII: HPS ranges for the engineered transition model.

parameter	range
$\lambda$ stddev	[0.0001, 0.001, 0.01]
$\sigma$ stddev	[0.0001, 0.001, 0.01]
$\tilde{\lambda}$ stddev	[0.0001, 0.001, 0.01]

APPENDIX E  
 FURTHER INFERENCE EXAMPLES

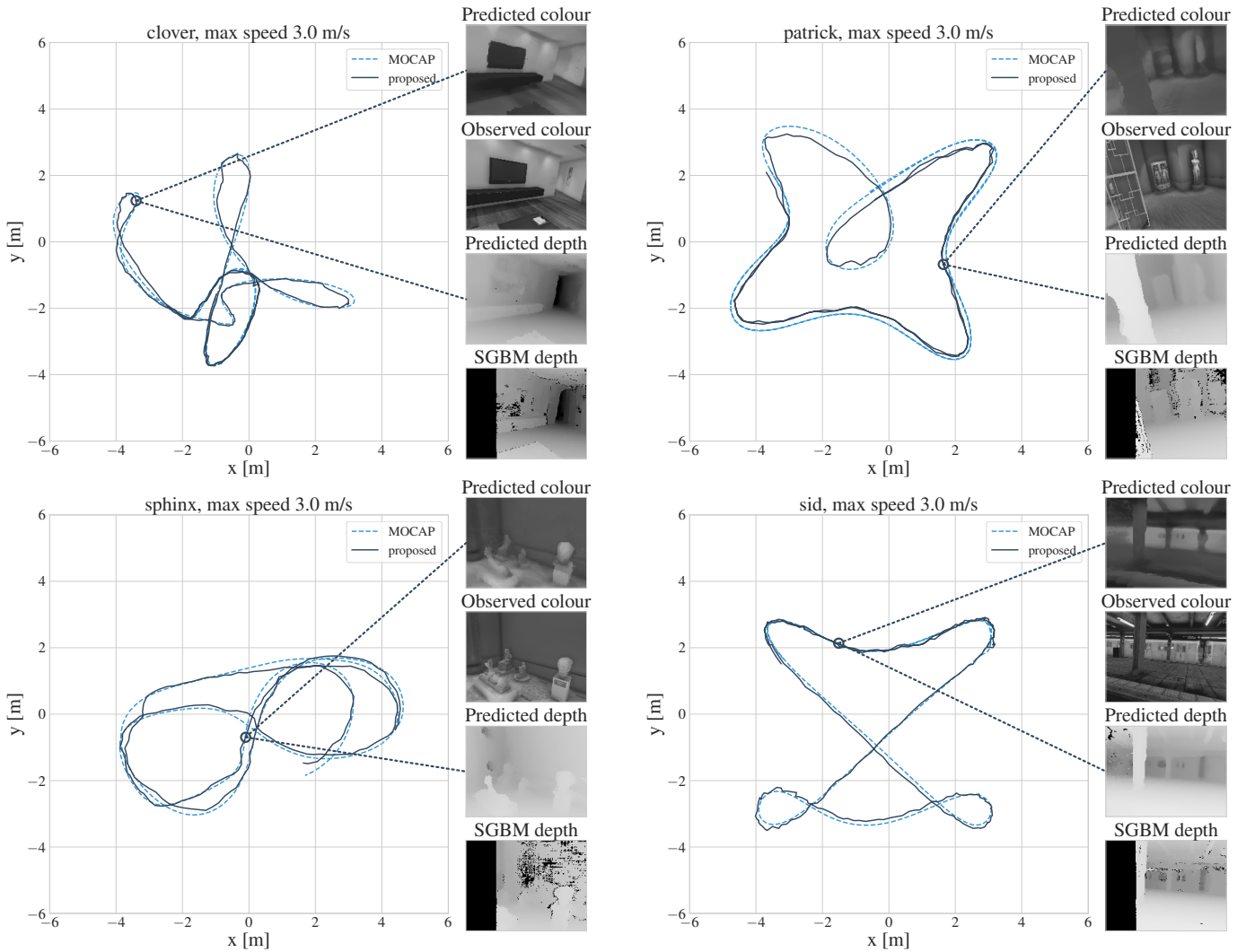


Fig. 9: Examples of inference in the full spatial model, expressed in localisation and mapping for segments of the following trajectories: *clover*, forward yaw, max speed 3.0m/s, *patrick*, forward yaw, max speed 3.0m/s, *sphinx*, forward yaw, max speed 3.0m/s and *sid*, forward yaw, max speed 3.0m/s. Left on every subfigure: top-down view of the localisation estimate. Right on every subfigure: depth and colour reconstructions from the generative model for one time step.

APPENDIX F  
DATA SET SPLITS

TABLE VIII: Lists of the trajectories in each of the data set splits, specifying the total number of pre-processed steps and the overall flight duration

Test set		
trajectory	# steps	duration [s]
star, constant yaw, 1.0 m/s	2680	268.0
star, constant yaw, 2.0 m/s	2635	263.5
star, constant yaw, 3.0 m/s	2640	264.0
star, constant yaw, 4.0 m/s	2667	266.7
star, constant yaw, 5.0 m/s	2611	261.1
star, forward yaw, 1.0 m/s	833	83.3
star, forward yaw, 2.0 m/s	1503	150.3
star, forward yaw, 3.0 m/s	1523	152.3
star, forward yaw, 4.0 m/s	1627	162.7
star, forward yaw, 5.0 m/s	1108	110.8
picasso, constant yaw, 1.0 m/s	2040	204.0
picasso, constant yaw, 2.0 m/s	2071	207.1
picasso, constant yaw, 3.0 m/s	2072	207.2
picasso, constant yaw, 4.0 m/s	2109	210.9
picasso, constant yaw, 5.0 m/s	2626	262.6
picasso, forward yaw, 1.0 m/s	833	83.3
picasso, forward yaw, 3.0 m/s	2083	208.3
picasso, forward yaw, 4.0 m/s	2057	205.7
picasso, forward yaw, 5.0 m/s	891	89.1
Validation set		
trajectory	# steps	duration [s]
sid, constant yaw, 1.0 m/s	2688	268.8
sid, constant yaw, 2.0 m/s	2677	267.7
sid, constant yaw, 3.0 m/s	833	83.3
sid, constant yaw, 4.0 m/s	2668	266.8
sid, constant yaw, 5.0 m/s	2661	266.1
sid, forward yaw, 1.0 m/s	897	89.7
sid, forward yaw, 2.0 m/s	1109	110.9
sid, forward yaw, 3.0 m/s	833	83.3
sid, forward yaw, 4.0 m/s	1109	110.9
sid, forward yaw, 5.0 m/s	1110	111.0
sphinx, constant yaw, 1.0 m/s	2612	261.2
sphinx, constant yaw, 2.0 m/s	2601	260.1
sphinx, constant yaw, 3.0 m/s	833	83.3
sphinx, constant yaw, 4.0 m/s	2560	256.0
sphinx, forward yaw, 1.0 m/s	1088	108.8
sphinx, forward yaw, 2.0 m/s	1087	108.7
sphinx, forward yaw, 3.0 m/s	833	83.3
sphinx, forward yaw, 4.0 m/s	1086	108.6
bentDice, constant yaw, 1.0 m/s	2624	262.4

bentDice, constant yaw, 2.0 m/s	2698	269.8
bentDice, constant yaw, 3.0 m/s	417	41.7
bentDice, constant yaw, 4.0 m/s	2632	263.2
bentDice, forward yaw, 1.0 m/s	1088	108.8
bentDice, forward yaw, 2.0 m/s	1088	108.8
bentDice, forward yaw, 3.0 m/s	833	83.3
patrick, constant yaw, 1.0 m/s	2598	259.8
patrick, constant yaw, 2.0 m/s	2584	258.4
patrick, constant yaw, 3.0 m/s	417	41.7
patrick, constant yaw, 4.0 m/s	2611	261.1
patrick, constant yaw, 5.0 m/s	2580	258.0
patrick, forward yaw, 1.0 m/s	1089	108.9
patrick, forward yaw, 2.0 m/s	1089	108.9
patrick, forward yaw, 3.0 m/s	833	83.3
patrick, forward yaw, 4.0 m/s	1091	109.1

Training set		
trajectory	# steps	duration [s]
3dFigure8, constant yaw, 1.0 m/s	2087	208.7
3dFigure8, constant yaw, 2.0 m/s	2130	213.0
3dFigure8, constant yaw, 3.0 m/s	2091	209.1
3dFigure8, constant yaw, 4.0 m/s	2136	213.6
3dFigure8, constant yaw, 5.0 m/s	2240	224.0
ampersand, constant yaw, 1.0 m/s	2086	208.6
ampersand, constant yaw, 2.0 m/s	2061	206.1
ampersand, constant yaw, 3.0 m/s	833	83.3
clover, constant yaw, 1.0 m/s	2575	257.5
clover, constant yaw, 2.0 m/s	2605	260.5
clover, constant yaw, 3.0 m/s	833	83.3
clover, constant yaw, 4.0 m/s	2631	263.1
clover, constant yaw, 5.0 m/s	2607	260.7
dice, constant yaw, 2.0 m/s	2605	260.5
dice, constant yaw, 3.0 m/s	833	83.3
dice, constant yaw, 4.0 m/s	2614	261.4
figure8, constant yaw, 1.0 m/s	1513	151.3
figure8, constant yaw, 2.0 m/s	2052	205.2
figure8, constant yaw, 5.0 m/s	1999	199.9
mouse, constant yaw, 1.0 m/s	2641	264.1
mouse, constant yaw, 2.0 m/s	2674	267.4
mouse, constant yaw, 3.0 m/s	833	83.3
mouse, constant yaw, 4.0 m/s	2620	262.0
mouse, constant yaw, 5.0 m/s	2655	265.5
oval, constant yaw, 2.0 m/s	2033	203.3
oval, constant yaw, 3.0 m/s	833	83.3
oval, constant yaw, 4.0 m/s	2035	203.5
thrice, constant yaw, 1.0 m/s	2726	272.6
thrice, constant yaw, 2.0 m/s	2658	265.8
thrice, constant yaw, 3.0 m/s	2656	265.6
thrice, constant yaw, 4.0 m/s	2656	265.6
thrice, constant yaw, 5.0 m/s	2621	262.1



tiltedThrice, constant yaw, 1.0 m/s	2624	262.4
tiltedThrice, constant yaw, 2.0 m/s	2624	262.4
tiltedThrice, constant yaw, 3.0 m/s	833	83.3
tiltedThrice, constant yaw, 4.0 m/s	2602	260.2
tiltedThrice, constant yaw, 5.0 m/s	2574	257.4
winter, constant yaw, 1.0 m/s	2625	262.5
winter, constant yaw, 2.0 m/s	2570	257.0
winter, constant yaw, 3.0 m/s	833	83.3
winter, constant yaw, 4.0 m/s	2569	256.9
winter, constant yaw, 5.0 m/s	2620	262.0
ampersand, forward yaw, 1.0 m/s	1100	110.0
ampersand, forward yaw, 2.0 m/s	893	89.3
clover, forward yaw, 1.0 m/s	1088	108.8
clover, forward yaw, 2.0 m/s	1088	108.8
clover, forward yaw, 3.0 m/s	833	83.3
clover, forward yaw, 4.0 m/s	1101	110.1
clover, forward yaw, 5.0 m/s	1091	109.1
dice, forward yaw, 1.0 m/s	1096	109.6
dice, forward yaw, 2.0 m/s	1099	109.9
dice, forward yaw, 3.0 m/s	833	83.3
mouse, forward yaw, 1.0 m/s	1110	111.0
mouse, forward yaw, 2.0 m/s	1107	110.7
mouse, forward yaw, 3.0 m/s	833	83.3
mouse, forward yaw, 4.0 m/s	1108	110.8
mouse, forward yaw, 5.0 m/s	1107	110.7
oval, forward yaw, 1.0 m/s	1086	108.6
oval, forward yaw, 2.0 m/s	892	89.2
oval, forward yaw, 3.0 m/s	833	83.3
oval, forward yaw, 4.0 m/s	1086	108.6
thrice, forward yaw, 1.0 m/s	1088	108.8
thrice, forward yaw, 2.0 m/s	1088	108.8
thrice, forward yaw, 3.0 m/s	833	83.3
thrice, forward yaw, 4.0 m/s	1088	108.8
thrice, forward yaw, 5.0 m/s	1088	108.8
tiltedThrice, forward yaw, 1.0 m/s	898	89.8
tiltedThrice, forward yaw, 2.0 m/s	1088	108.8
tiltedThrice, forward yaw, 3.0 m/s	833	83.3
tiltedThrice, forward yaw, 4.0 m/s	1088	108.8
tiltedThrice, forward yaw, 5.0 m/s	1087	108.7
winter, forward yaw, 2.0 m/s	1089	108.9
winter, forward yaw, 3.0 m/s	833	83.3
winter, forward yaw, 4.0 m/s	1091	109.1

---